

Three-dimensional imaging of targets buried in a cluttered semi-infinite medium

Ting Zhang, Patrick C. Chaumet, Anne Sentenac, and Kamal Belkebir

Citation: [Journal of Applied Physics](#) **114**, 143101 (2013); doi: 10.1063/1.4824282

View online: <http://dx.doi.org/10.1063/1.4824282>

View Table of Contents: <http://scitation.aip.org/content/aip/journal/jap/114/14?ver=pdfcov>

Published by the [AIP Publishing](#)

Articles you may be interested in

[Experimental microwave imaging of three-dimensional targets with different inversion procedures](#)

J. Appl. Phys. **106**, 034901 (2009); 10.1063/1.3183939

[A Hyperbolic Penalty Filter Method for Semi-Infinite Programming](#)

AIP Conf. Proc. **1048**, 269 (2008); 10.1063/1.2990909

[Iterative three-dimensional expectation maximization restoration of single photon emission computed tomography images: Application in striatal imaging](#)

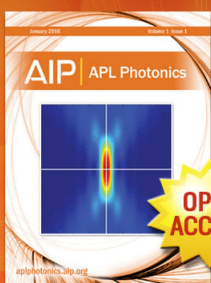
Med. Phys. **33**, 52 (2006); 10.1118/1.2135908

[Semiautomatic three-dimensional segmentation of the prostate using two-dimensional ultrasound images](#)

Med. Phys. **30**, 887 (2003); 10.1118/1.1568975

[Three-dimensional tomosynthetic image restoration for brachytherapy source localization](#)

Med. Phys. **28**, 1812 (2001); 10.1118/1.1388906



Launching in 2016!

The future of applied photonics research is here

OPEN
ACCESS

AIP | APL
Photonics

Three-dimensional imaging of targets buried in a cluttered semi-infinite medium

Ting Zhang, Patrick C. Chaumet, Anne Sentenac, and Kamal Belkebir

Institut Fresnel (UMR 7249), Av. Escadrille Normandie-Niemen, F-13397 Marseille cedex 20, France

(Received 16 July 2013; accepted 18 September 2013; published online 7 October 2013)

The present contribution deals with the detection and characterization of targets embedded in a highly cluttered environment using an electromagnetic wave probing. The targets are buried in a semi-infinite host medium with a flat interface and random permittivity. A two-dimensional antenna array is located in air above the random medium for illuminating and detecting the scene. The poor impedance matching between the antennas and the host medium limits significantly the effective numerical aperture of the imaging system. To reconstruct the targets, we propose to combine the DORT (french acronym for *Décomposition de l'Opérateur de Retournement Temporel*) method with an iterative inversion technique and a frequency hopping procedure. Numerical experiments show that this approach permits the reconstruction of the targets even when they are located in a highly cluttered medium. © 2013 AIP Publishing LLC. [<http://dx.doi.org/10.1063/1.4824282>]

I. INTRODUCTION

The objective of electromagnetic inverse scattering problems is to determine intrinsic properties, i.e., localization, shapes and constitutive materials, of objects from the knowledge of their responses to electromagnetic excitation. Intensive research activities have been carried out in the last decades to provide efficient algorithms able to solve such ill-posed and non-linear problems.^{1–4} In practical applications, such as sub-soil probing, these techniques do not distinguish the possible inhomogeneities of the host medium from the targets themselves and endeavour to reconstruct the whole permittivity distribution. This strategy yields to a poor estimation of the target.⁵

On the other hand, many studies were devoted to understanding the clutter influence in the deterioration of the signal-response of targets. Many procedures were proposed to reduce the clutter-signal ratio. Thus, the correlation of scattered fields with respect to a configuration parameter (wavelength, incidence angle, and antenna position)⁶ permits to reduce the influence of the clutter or that of the roughness of the surface separating the embedding medium and the measurement medium.^{7–9} Other techniques for diminishing the clutter influence take advantage of the properties of the Time Reversal (TR) operator which have been studied in acoustic^{10–12} and electromagnetic domains.^{13–17} They usually perform the Singular Value Decomposition (SVD) of the TR operator and either work on the noise sub-space (as in the Multiple signal classification (MUSIC) method¹⁸) or on the signal subspace as in the DORT (*décomposition de l'opérateur de retournement temporel*) method for detecting and locating targets in noisy medium. The sensitivities of the MUSIC and the DORT algorithms have been compared in Ref. 19.

In DORT, the number of scatterers is deduced from the leading singular values of the TR operator. The corresponding eigenvectors feeding the antenna array as currents permit one to focus onto each scatterer and thus to locate

it.^{5,13,14,20–22} DORT can be applied to the full time-domain operator²³ or to the monochromatic (on the central based frequency) TR operator. In addition to the probing wavelength, the localization accuracy depends basically on the solid angle under which the targets are seen by the imaging system. The larger this solid angle the better the resolution.^{24,25}

Recently, it was shown that combining DORT with an hybrid inversion algorithm could greatly improve the detection, localization and characterization of targets buried in random medium as compared to DORT or the inversion procedure alone.²⁶ This study was conducted in a simplified configuration in which the antennas are plunged into the probing medium so that the impedance matching is perfect. In this work, we analyze the hybrid-DORT approach in a more realistic situation (which is encountered for example in medical imaging, mineral exploration or through-wall imaging) where a flat interface separates the homogeneous medium (the air) containing the antennas, from another semi-infinite medium embedding the targets, see Sec. II. The main difficulty of this configuration is that the high reflectivity of the host medium limits significantly the angular excursion of the field radiated by the antennas below the interface. The effective numerical aperture of the imager, which measures the solid angle under which the targets are illuminated and observed, is about one third of that of the ideal configuration presented in Ref. 26. As a consequence, the DORT ability for focusing on the targets and the imaging performance of the inversion technique are likely to be deteriorated, especially in the direction normal to the interface.¹³ To ameliorate the results, we propose to use multifrequency data and implement a frequency hopping method in the reconstruction scheme. Our imaging approach is checked on synthetic data.

Section III A describes the rigorous electromagnetic wave solver that simulates the field scattered by the targets in the half-space configuration. Section III B 1 explains the inversion method and Sec. III B 2 shows how it is combined to the DORT approach. Section IV details the numerical

experiments and analyses the influence of the clutter on the reconstructions.

II. PROBLEM CONFIGURATION

The geometry of the problem is depicted in Fig. 1. The imaging system consists in a square array (of side size of $8\lambda_{\text{ref}}$) of crossed-dipole antennas lying in the plane $z = 2\lambda_{\text{ref}}$. The upper medium of relative permittivity 1 is separated from the lower semi-infinite medium by a flat interface at $z = \lambda_{\text{ref}}$, λ_{ref} being the wavelength of the radiated electromagnetic field of dipoles in the vacuum at the frequency $f_{\text{ref}} = 500$ MHz. The three-dimensional targets under study of relative permittivity distribution $\epsilon_r(\mathbf{r})$ are embedded in the lower medium and entirely confined in a large box of volume ($L_x \times L_y \times L_z$), in which the relative permittivity $\epsilon_g(\mathbf{r})$ fluctuates as

$$\epsilon_g(\mathbf{r}) = \epsilon_b + \epsilon_c(\mathbf{r}), \quad (1)$$

where the average relative permittivity of the background medium is denoted by ϵ_b and $\epsilon_c(\mathbf{r})$ is a random function representing the clutter (structural noise) with null average over the domain W . The entire configuration is non-magnetic. The measurements are carried out in the bi-static mode where each antenna can play the role of transmitter and receiver. Furthermore, the dipole antenna which generates the electromagnetic incident field and receivers can take the three orientations along the x -axis, y -axis, or z -axis.

III. FORWARD AND INVERSE SCATTERING PROBLEM

The forward and inverse scattering method is very similar to that presented in Ref. 26. The sole difference lays in the Green dyadic functions. In Ref. 26, they represented the field radiated by a dipole in a homogeneous medium while, in this work, they represent the field radiated by a dipole located in a semi-infinite medium.

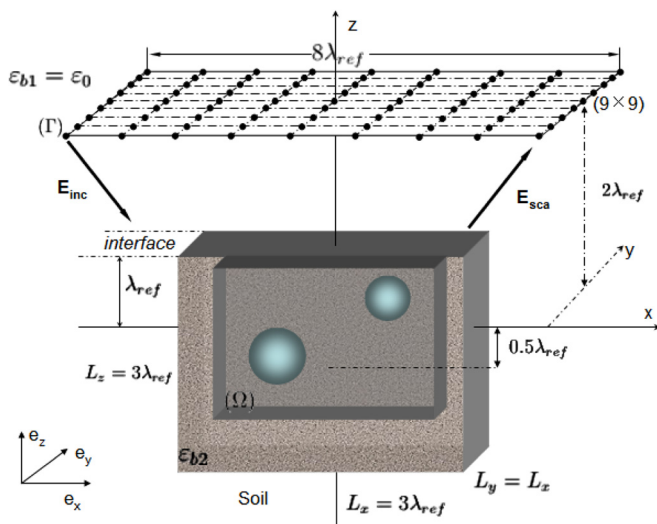


FIG. 1. Geometry of imaging configuration. The targets are embedded in a semi-infinite host medium with a flat interface. The imaging system is constituted of 81 transmitters and receivers placed on a two-dimensional lattice with square mesh. The antennas array is located at two wavelengths above the flat surface of the host medium. The typical size of the targets is about one incident wavelength.

A. Forward scattering problem

To model the forward scattering problem, we use the coupled dipole method (CDM) which is equivalent to a Method of Moment (MoM).²⁷ In the CDM, objects of permittivity $\epsilon_r(\mathbf{r})$ are subdivided onto an array of N polarizable subunits. The macroscopic field at each subunit of discretization, $\mathbf{E}(\mathbf{r}_i)$, is expressed with the following self-consistence equation:²⁷

$$\mathbf{E}(\mathbf{r}_i) = \mathbf{E}^{\text{inc}}(\mathbf{r}_i) + \sum_{j=1}^N \mathbf{G}(\mathbf{r}_i, \mathbf{r}_j) \chi(\mathbf{r}_j) \mathbf{E}(\mathbf{r}_j), \quad (2)$$

where $\chi(\mathbf{r}_j) = \epsilon_r(\mathbf{r}_j) - \epsilon_b$ is the contrast of the permittivity distribution, $\mathbf{E}^{\text{inc}}(\mathbf{r}_i)$ denotes the incident field at the subunit i and \mathbf{G} is dyadic Green function that takes into account the interaction with the substrate.^{28,29} Once Eq. (2) is solved, the scattered field $\mathbf{E}^{\text{sca}}(\mathbf{r})$ at an arbitrary position \mathbf{r} reads as

$$\mathbf{E}^{\text{sca}}(\mathbf{r}) = \sum_{j=1}^N \mathbf{G}(\mathbf{r}, \mathbf{r}_j) \chi(\mathbf{r}_j) \mathbf{E}(\mathbf{r}_j). \quad (3)$$

B. The inverse scattering problem

1. The hybrid method

The inverse problem consists in finding parameters of interest of buried objects, namely the permittivity distribution, inside a bounded investigating (or test) domain $\Omega \subset W$. Many iterative methods have been developed for solving such ill-posed and non linear problems. The basic idea underlying these iterative techniques is to adjust gradually the permittivity distribution within the investigating domain Ω , such that the associated scattered field \mathbf{E}^{sca} to the known incident field \mathbf{E}^{inc} matches the measured scattered field \mathbf{f} . In our configuration, objects under study are illuminated successively by $l = 1, \dots, L$ antennas where each antenna can be oriented along the x , y and z axis. It means that objects under study are illuminated by $3L$ incident waves. For the sake of simplicity, Eqs. (2) and (3) are rewritten in a more condensed form using the notation of operators

$$\mathbf{E}_{l,\alpha} = \mathbf{E}_{l,\alpha}^{\text{inc}} + \mathbf{A} \chi \mathbf{E}_{l,\alpha} \quad \text{and} \quad \mathbf{E}_{l,\alpha}^{\text{sca}} = \mathbf{B} \chi \mathbf{E}_{l,\alpha}, \quad (4)$$

where $\alpha = x, y$ or z represent the orientation of antennas. Note that \mathbf{A} and \mathbf{B} do not depend on the incidence field. The Hybrid Method (HM) is used for solving the inverse scattering problem. This technique which has been developed first for the two-dimensional case in Refs. 30 and 31, minimizes a cost function at an iteration step n of the form

$$\mathcal{F}_n(\chi_n, \mathbf{E}_{l,\alpha,n}) = \frac{\sum_{\alpha} \sum_{l=1}^L \sum_{x,y,z} \|\mathbf{f}_{l,\alpha} - \mathbf{B} \chi_n \mathbf{E}_{l,\alpha,n}\|_{\Gamma}^2}{\sum_{\alpha} \sum_{l=1}^L \sum_{x,y,z} \|\mathbf{f}_{l,\alpha}\|_{\Gamma}^2} + \frac{\sum_{\alpha} \sum_{l=1}^L \sum_{x,y,z} \|\mathbf{E}_{l,\alpha}^{\text{inc}} - \mathbf{E}_{l,\alpha,n} + \mathbf{A} \chi_n \mathbf{E}_{l,\alpha,n}\|_{\Omega}^2}{\sum_{\alpha} \sum_{l=1}^L \sum_{x,y,z} \|\mathbf{E}_{l,\alpha}^{\text{inc}}\|_{\Omega}^2}. \quad (5)$$

Prior information, stating that both the imaginary part of the relative permittivity and the electrical susceptibility of targets are non negative, is included in the inversion scheme. This accomplished by instead of retrieving the complex function χ_n , two real auxiliary functions ξ_n and η_n are reconstructed such that

$$\chi_n = 1 + \xi_n^2 + j\eta_n^2 - \varepsilon_b, \quad (6)$$

where η^2 represents the imaginary part of the relative permittivity of reconstructed targets while ξ^2 denotes the electrical susceptibility of targets. Hence, three sequences related to ξ , η and to the complex field $\mathbf{E}_{l,\alpha}$ inside the investigating domain Ω , are build up according to the following recursive relations

$$\xi_n = \xi_{n-1} + \beta_{n;\xi} d_{n;\xi}, \quad (7)$$

$$\eta_n = \eta_{n-1} + \beta_{n;\eta} d_{n;\eta}, \quad (8)$$

$$\mathbf{E}_{l,\alpha,n} = \mathbf{E}_{l,\alpha,n-1} + a_{l,\alpha,n}^v \mathbf{v}_{l,\alpha,n} + a_{l,\alpha,n}^w \mathbf{w}_{l,\alpha,n}, \quad (9)$$

where $\mathbf{v}_{l,\alpha,n}$, $\mathbf{w}_{l,\alpha,n}$, $d_{n;\xi}$ and $d_{n;\eta}$ are updating directions with respect to the total field $\mathbf{E}_{l,\alpha}$, and to ξ and η , respectively. The scalar coefficients $a_{l,\alpha,n}^v$, $a_{l,\alpha,n}^w$ and β_n are weights that are determined at each iteration step n such that they minimize the normalized cost functional given in Eq. (5). Substituting expression of χ_n in the cost function of Eq. (5) with expressions of Eqs. (7)–(9) leads to a polynomial form of the cost function with respect to the weighting coefficients $\beta_{n;\xi}$, $\beta_{n;\eta}$, $a_{l,\alpha,n}^v$ and $a_{l,\alpha,n}^w$. The minimization of the cost function is numerically performed using the well-known Polak-Ribière conjugate gradient procedure.³²

2. The hybrid-DORT method

For each source l ($l = 1, \dots, L$), oriented along α -direction, the scattered vector field, assuming that each antenna can play the role of the source and the receiver, is measured at $l = 1, \dots, L$ receivers with its three field components. Hence, a $3L \times 3L$ symmetric matrix is built, denoted by \mathbf{K} as well as the TRO defined as the self-adjoint matrix $\mathbf{L} = \mathbf{K}^\dagger \mathbf{K}$. Eigenvalues and eigenvectors of \mathbf{L} permit to localize the brightest scatterers and to synthesize a wave focusing selectively on each scatterer.^{13,14,33}

The hybrid-DORT method consists in using the focusing wave in the inversion algorithm.²⁶ Let us assume that the DORT method yields $\zeta = 1, \dots, N_{\text{ev}}$ relevant eigenvalues. One builds the focusing waves $\mathbf{E}_\zeta^{\text{inc;DORT}}$ from the associated eigenvectors $\mathbf{V}(\zeta)$,

$$\mathbf{E}_\zeta^{\text{inc;DORT}}(\mathbf{r}) = \sum_{l=1}^L \sum_{\alpha} V_{l,\alpha}(\zeta) \mathbf{E}_{l,\alpha}^{\text{inc}}(\mathbf{r}), \quad (10)$$

where $V_{l,\alpha}(\zeta)$ denotes the l -th component and α orientation of the eigenvector $\mathbf{V}(\zeta)$ associated with the eigenvalue ζ and $\mathbf{E}_{l,\alpha}^{\text{inc}}(\mathbf{r})$ is the field radiated by a unit amplitude dipole α -oriented located at the receiver l position and observed at \mathbf{r} . Due to the linearity of the Maxwell equations, the scattered field that would be measured with the incident fields

$\mathbf{E}_\zeta^{\text{inc;DORT}}$ follows similar linear combination as the one used in Eq. (10). The scattered field $\mathbf{E}_\zeta^{\text{sca;DORT}}$ at the position \mathbf{r} reads,

$$\mathbf{E}_\zeta^{\text{sca;DORT}}(\mathbf{r}) = \sum_{l=1}^L \sum_{\alpha} V_{l,\alpha}(\zeta) \mathbf{f}_{l,\alpha}(\mathbf{r}), \quad (11)$$

where $\mathbf{f}_{l,\alpha}$ is the original scattered field, i.e., the data provided by the scattering experiment and from which the DORT method is applied. The utilization of the information derived from DORT method in HM is achieved in practice by minimizing a cost function involving $\mathbf{E}_\zeta^{\text{inc;DORT}}$ and $\mathbf{E}_\zeta^{\text{sca;DORT}}$ instead of $\mathbf{E}_{l,\alpha}^{\text{inc}}$ and $\mathbf{f}_{l,\alpha}$. The minimized cost function reads,

$$\mathcal{F}_n^{\text{DORT}}(\chi_n, \mathbf{E}_{\zeta,n}) = \frac{\sum_{\zeta=1}^{N_{\text{ev}}} \|\mathbf{f}_\zeta^{\text{sca;DORT}} - \mathbf{B}_{\chi_n} \mathbf{E}_{\zeta,n}\|_\Gamma^2}{\sum_{\zeta=1}^{N_{\text{ev}}} \|\mathbf{f}_\zeta^{\text{sca;DORT}}\|_\Gamma^2} + \frac{\sum_{\zeta=1}^{N_{\text{ev}}} \|\mathbf{E}_\zeta^{\text{inc;DORT}} - \mathbf{E}_{\zeta,n} + \mathbf{A}_{\chi_n} \mathbf{E}_{\zeta,n}\|_\Omega^2}{\sum_{\zeta=1}^{N_{\text{ev}}} \|\mathbf{E}_\zeta^{\text{inc;DORT}}\|_\Omega^2}. \quad (12)$$

Notice that for the inversion without using DORT, the minimized cost function \mathcal{F}_n is a non-linear expression with respect to $6L$ complex variables $a_{l,\alpha,n}$ and two real valued variables $(\beta_{n;\xi}, \beta_{n;\eta})$, while using the DORT method, the minimized cost function $\mathcal{F}_n^{\text{DORT}}$ depends only on $2N_{\text{ev}}$ complex unknown $a_{\zeta,n}$ and two real valued variables $(\beta_{n;\xi}, \beta_{n;\eta})$. Subsequently, the computational time decreases drastically when the DORT method is used.

IV. NUMERICAL EXPERIMENTS

In this section, we analyze the performance of the Hybrid-DORT method to localize and characterize buried targets in a highly cluttered environment. All the data are obtained with the CDM forward solver. The mesh size of the scattering domain is $a = \lambda_{\text{ref}}/18$ where $\lambda_{\text{ref}} = 0.6$ m is the wavelength in vacuum of an impinging wave at the reference frequency $f_{\text{ref}} = 500$ MHz. The flat interface separating the measurement medium (air) and the host medium (dry soil of relative permittivity $\varepsilon_b = 3$) where the targets are buried in is at $z = \lambda_{\text{ref}}$. The targets are confined entirely in a large box W of volume $(3\lambda_{\text{ref}} \times 3\lambda_{\text{ref}} \times 3\lambda_{\text{ref}}) \text{ m}^3$ which is placed beneath the interface. The scattering domain W is centered at $(0, 0, -0.5\lambda_{\text{ref}})$. The measurement surface Γ is a lattice of $L = 81$ independent antennas regularly distributed on a square of side-size $8\lambda_{\text{ref}}$. Thus, the coupling between antennas is neglected. Each antenna plays either the role of an emitter or the role of a receiver. The antennas square array Γ lays at λ_{ref} above the interface as shown in Fig. 1.

The investigating domain $\Omega \subset W$ introduced in the inversion procedure is discretized with a mesh size of $a =$

$\lambda_{\text{ref}}/10$ which is almost twice larger than the mesh size $a = \lambda_{\text{ref}}/18$ used to generate the synthetic data. Note that in all the experiments, the losses of the targets and random medium are neglected in the forward model and the reconstructed imaginary part of the relative permittivity is always very small. Hence, only the real part of the reconstructed permittivities is presented. To quantify the quality of the reconstruction we define a contrast reconstruction error as

$$\text{Err}_\chi = \frac{\|\chi_{\text{actual}} - \chi_{\text{rec}}\|_{\Omega}^2}{\|\chi_{\text{actual}}\|_{\Omega}^2}, \quad (13)$$

where χ_{actual} is the relative permittivity contrast distribution of the actual objects, while χ_{rec} is the reconstructed one.

A. Reconstruction of a target without clutter

We start the analysis of our approach with the ideal configuration of two spheres of relative permittivity $\epsilon_r = 5$ buried in a homogeneous half-space. The smallest sphere, with radius $r_1 = \lambda_{\text{ref}}/8$, located at $(0.5\lambda_{\text{ref}}, 0.4\lambda_{\text{ref}}, 0.5\lambda_{\text{ref}})$, is closer to the interface than the largest sphere of radius $r_2 = \lambda_{\text{ref}}/6$ and centered at $(-0.5\lambda_{\text{ref}}, 0.4\lambda_{\text{ref}}, -0.5\lambda_{\text{ref}})$.

We first display in Fig. 2 the intensity of the fields in W derived from the DORT eigenvectors for the first and third eigenvalues. Similar intensities are obtained for the second and the fourth eigenvalues. It is observed that the eigenvectors corresponding to the first and the second eigenvalue synthesize a wave focusing onto the scatterer near the interface while the eigenvectors corresponding to the third and the fourth eigenvalue focus on the largest sphere far from the interface. The other eigenvectors do not yield any focusing fields. Note that, due to the limited effective numerical aperture of the imager in the half-space configuration, the number of eigenvalues associated to each scatterer is smaller than that of the homogeneous configuration (two instead of three)^{25,26} and the focusing ability in the direction normal to the interface is significantly deteriorated.

From the DORT intensities maps, one can restrict the investigating domain Ω to be used in the inversion to a volume of $(2\lambda_{\text{ref}} \times \lambda_{\text{ref}} \times 2\lambda_{\text{ref}}) \text{ m}^3$, centered at $(0, 0.4\lambda_{\text{ref}}, 0)$. The volume of this box is $4\lambda_{\text{ref}}^3$, about seven times smaller than the scattering domain W used in the forward scattering problem to generate the data.

Figure 3(a) shows the reconstruction obtained at λ_{ref} using the hybrid inversion method with the DORT focusing approach. Hereafter the hybrid-DORT method will be called HDORTM. The reconstruction exhibits ghost objects along the z -direction which are particularly visible on the axial cut of the reconstructed profile plotted in Figs. 3(c) and 3(d). The low value of the cost function shows that these replica located along the z -axis with a periodicity about $\lambda_{\text{ref}}/2$ provide the same scattered field than that of the actual scatterer. This oscillating behavior is a direct consequence of the limited numerical aperture of the imaging system and has been largely studied in the two-dimensional configuration.⁵ To compensate for the lack of information due to the small numerical aperture of the imaging system, we used multifrequency polychromatic data and applied the frequency-hopping approach as described in Ref. 5. It consists in reconstructing the targets with a low frequency data and using the result as an initial guess for performing the inversion at higher frequency. We simulated the data for three different incident wavelengths $\lambda_1 = 3\lambda_{\text{ref}}$, $\lambda_2 = 1.5\lambda_{\text{ref}}$ and λ_{ref} . Note that these supplementary illuminations do not increase the numerical aperture of imager and do not provide higher spatial frequencies information. The result of the frequency-hopping approach is shown in Fig. 3. The two scatterers are now satisfactorily reconstructed both in shape and permittivity estimation and the oscillating behavior of the estimated permittivity has disappeared.

B. Reconstruction in a cluttered medium

We now investigate the influence of clutter on the imaging performance. We consider the same configuration as previously, but the targets are now buried in a cluttered

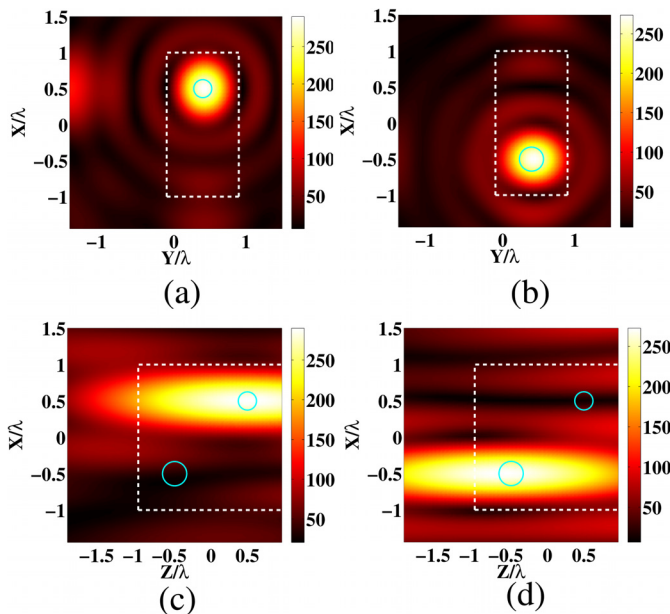


FIG. 2. Intensity map within W domain of the electric field deduced from the eigenvectors corresponding to the first ((a) and (c)) and the third ((b) and (d)) eigenvalue. (a) in the (x,y) plane for $z = 0.5\lambda_{\text{ref}}$. (b) in the (x,y) plane for $z = -0.5\lambda_{\text{ref}}$. (c) and (d) in the (x,z) plane for $y = 0.4\lambda_{\text{ref}}$. Circles represent the actual boundary profiles of targets, while the dashed box represents the investigating domain Ω to be used in the inversion procedure.

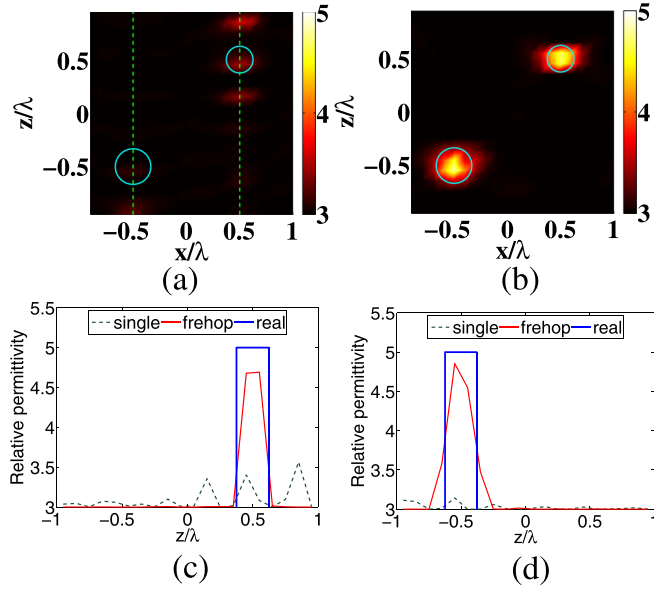


FIG. 3. Permittivity reconstruction obtained by HDORTM when the targets are placed in a homogeneous semi-infinite medium. (a) Cut along the (x,z) plane for $y = 0.4\lambda_{\text{ref}}$ when sole the data corresponding to $\lambda = \lambda_{\text{ref}}$ are used. (b) Same as (a), but the frequency hopping procedure has been applied. (c) Plot of the relative permittivity along a vertical line passing through the target close to the interface (corresponding to $x = 0.5\lambda_{\text{ref}}$ and $y = 0.4\lambda_{\text{ref}}$). The solid curve indicates the actual permittivity profiles, the red line indicates the reconstruction obtained with the frequency hopping procedure, the dark green dashed line indicates the reconstruction obtained with the λ_{ref} data only. (d) same as (c) but the line passes through the target far from the interface at $x = -0.5\lambda_{\text{ref}}$ and $y = 0.4\lambda_{\text{ref}}$.

medium. The random permittivity of the clutter $\varepsilon_c(\mathbf{r})$ is assumed to be a zero mean Gaussian random variable with standard deviation σ_f and Gaussian correlation function $C(\mathbf{r})$ with the correlation length l_c .²⁶

$$C(\mathbf{r}) = \sigma_f^2 \exp\left(-\frac{\|\mathbf{r}\|^2}{l_c^2}\right), \quad (14)$$

$$\varepsilon_g(\mathbf{r}) = \varepsilon_b + \varepsilon_c(\mathbf{r}), \quad (15)$$

The ratio of clutter-to-signal (CSR) is defined as

$$\text{CSR} = \frac{\sum_{l=1}^N \sum_{\alpha} \|\mathbf{f}_{l,\alpha} - \mathbf{f}_{l,\alpha}^{\text{scatters}}\|_{\Gamma}^2}{\sum_{l=1}^N \sum_{\alpha} \|\mathbf{f}_{l,\alpha}^{\text{scatters}}\|_{\Gamma}^2}, \quad (16)$$

where $\mathbf{f}_{l,\alpha}$ and $\mathbf{f}_{l,\alpha}^{\text{scatters}}$ denote the field scattered by the targets with or without the clutter, respectively. In all reported examples the multiple scattering between the clutter and the targets is negligible. Yet, the computation of the scattered fields is carried out rigorously.

In the first example, we consider an quasi-unrelated clutter with standard deviation $\sigma_f = 0.058$ and $l_c = \lambda_{\text{ref}}/18$. the corresponding CSR is 6%, 16%, 102% at $\lambda_1 = 3\lambda_{\text{ref}}$, $\lambda_2 = 1.5\lambda_{\text{ref}}$, λ_{ref} , respectively. For all the wavelengths and even when the clutter-to-signal CSR is as high as 102%, the DORT method permits to localize the targets (the maps of

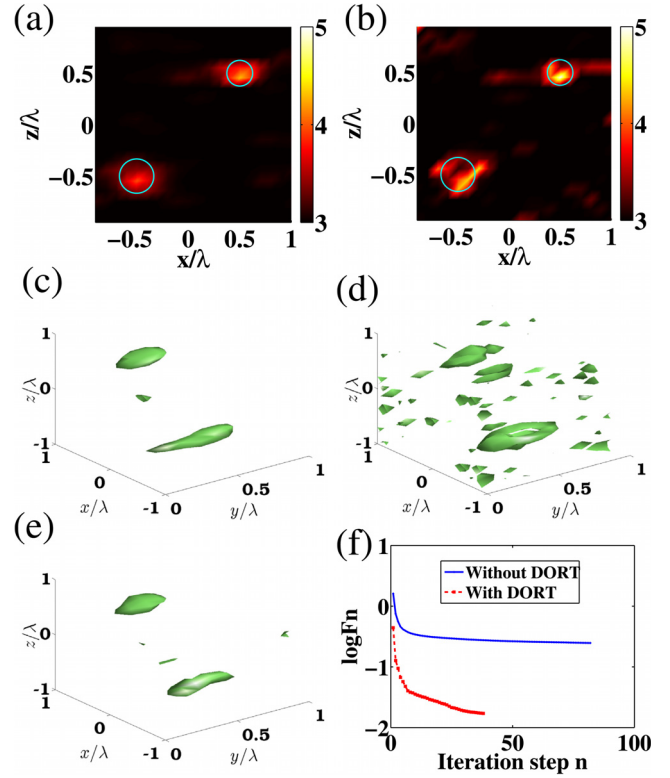


FIG. 4. Reconstructed permittivity using either the HDORTM approach or the HM. Both techniques are applied with the frequency-hopping procedure. The targets are buried in a quasi-unrelated cluttered medium with correlation length $l_c = \lambda_{\text{ref}}/18$ and standard variation $\sigma_f = 0.058$ yielding a CSR of 102%. Except indicated otherwise, the clutter is generated in a domain W of size $(3\lambda_{\text{ref}} \times 3\lambda_{\text{ref}} \times 3\lambda_{\text{ref}}) m^3$. (a) cut along the (x,z) plane at $y = 0.4\lambda_{\text{ref}}$ using the HDORTM. (b) same as (a) using the HM. (c) Iso-surface of the reconstructed permittivity profile at $\varepsilon = 3.5$ using HDORTM. (d) same as (c) using HM. (e) same as (c) but the clutter is generated in a larger domain W' of size $(6\lambda_{\text{ref}} \times 6\lambda_{\text{ref}} \times 3\lambda_{\text{ref}}) m^3$. (f) Evolution of the cost function (log-scale representation) versus the iteration step using HDORTM (dashed curve) and HM (solid curve).

the focusing waves are not shown). The reconstruction obtained using the hybrid-DORT method (HDORTM) and with the Hybrid Method (HM) alone is reported in Fig. 4. In both cases, the frequency hopping procedure is applied. The superiority of HDORTM is clearly seen. Using HM, bright scatterers are reconstructed in the entire volume of the investigating domain, blurring the targets signal and increasing the level of false alarms. With HDORTM [Fig. 4(c)] effects related to the presence of the clutter is remarkably diminished and only the two strong targets are retrieved. The quality of the reconstruction is quantitatively estimated by the reconstruction error of χ . Using HDORTM this error is about $\text{Err}_{\chi} = 66\%$ and raises up to $\text{Err}_{\chi} = 282\%$ when HM is used. The value of the cost function is one order of magnitude lower with HDORTM than the one obtained with HM, Fig. 4(f). Moreover, the computational time of HDORTM (which uses only 4 incident fields at each inversion) at the wavelength λ_{ref} is 287 s, about 80 times smaller than that of the HM 22201 s (which uses 81 incident fields).

It is worth noting that, although the clutter is accounted for only in the domain W , our numerical experiment can be used to infer the behavior of the imaging system in a realistic

situation where the clutter is present everywhere in the host medium. Indeed, its results do not change when the size of W is increased. We display in Fig. 4 the reconstruction obtained by HDORTM when W is multiplied by a factor of four to reach $(6\lambda_{\text{ref}} \times 6\lambda_{\text{ref}} \times 3\lambda_{\text{ref}}) \text{ m}^3$ (keeping the same clutter distribution in the initial W and the same statistics). In this case, the clutter to signal ratio is increased to 29%, 65%, and 325% at wavelengths $\lambda_1 = 3\lambda_{\text{ref}}$, $\lambda_2 = 1.5\lambda_{\text{ref}}$, λ_{ref} , respectively. Yet, the two scatterers are still well localized by DORT and the reconstructions are similar to those obtained with the small W with the same error $\text{Err}_\chi = 66\%$. The focusing property of DORT permits to diminish drastically the influence of the clutter far from the targets.

To evaluate the reproducibility of HDORTM, different distributions of clutter with the same statistical characteristics have been generated. The HDORTM yielded similar reconstructions with an average error Err_χ about 64% with a confidence interval of 3%. With the chosen clutter statistics, the performance of the HDORTM does not depend on the specific clutter distribution even in the vicinity of the targets.

C. Influence of the polarization of the incident field

In our configuration, the emitting and receiving antennas are oriented along three orientations, x -axis, y -axis and z -axis, respectively. In order to illustrate the necessity of using the vectorial configuration, we consider a simple configuration where the antennas are oriented along one single direction, x axis or y axis. With these scalar data, only one eigenvalue is associated with each strong scatterer. The reconstruction obtained from the scalar data with HDORTM is displayed as iso-surface in Fig. 5. We observe a clear deterioration of the image as compared to that obtained with the vectorial data, Fig. 4(c). The reconstruction error in the scalar case is $\text{Err}_\chi = 101\%$ and $\text{Err}_\chi = 96\%$ for the x and y orientations, respectively, to be compared to $\text{Err}_\chi = 66\%$ for the full polarized data.

D. Influence of the structural noise

1. Influence of the standard deviation

In this paragraph, we study the robustness of HDORTM and the frequency-hopping approach,^{34,35} with respect to the clutter strength. The correlation length l_c is kept fixed at

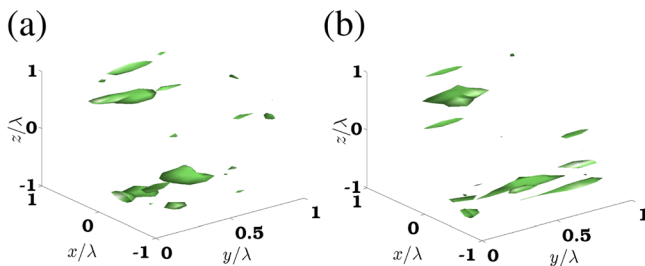


FIG. 5. Iso-surface of the reconstructed permittivity profile at $\varepsilon = 3.5$ using HDORTM for the same configuration as that used in Fig. 4 (c); (a) The antennas are oriented along the x direction and the scattered field is detected along the x direction only. (b) The antennas are oriented along the y direction and the scattered field is detected along the y direction only.

$\lambda_{\text{ref}}/18$, while the standard deviation is increased to $\sigma_f = 0.07$, leading to $\text{CSR} = 9\%$, 23% , and 148% for the wavelength $\lambda_1 = 3\lambda_{\text{ref}}$, $\lambda_2 = 1.5\lambda_{\text{ref}}$, λ_{ref} , respectively. Unsurprisingly, with such level of noise at λ_{ref} , the ability of DORT for focusing on the scatterers is deteriorated. In particular, the eigenvector corresponding to the fourth eigenvalue generates a wave that focuses both on the scatterer and on the clutter with the same intensity level. On the other hand, the data at $\lambda_2 = 1.5\lambda_{\text{ref}}$ are less noisy and yield DORT fields that focuses exclusively on the scatterers. Thus, we use the DORT intensity maps at $\lambda_2 = 1.5\lambda_{\text{ref}}$ for defining the investigating domain of the inversion procedure. In Fig. 6, we plot the reconstructed relative permittivity in (x, z) plane obtained at the wavelength λ_{ref} with the frequency hopping procedure. Due to the bad focalization of the fourth eigenvalue, sole the three incident fields associated to the three largest eigenvalues are used in the inversion procedure. The reconstruction of the two scatterers with HDORTM is similar to that displayed in Fig. 4(a) for the less noisy configuration. On the other hand, Fig. 4(b) shows that the reconstruction given by HM is totally blurred by the noise stemming from the clutter.

2. Influence of the correlation length

In this paragraph, the influence of the correlation length l_c on the reconstruction is analyzed. Hereafter, the standard deviation of the clutter $\sigma(\varepsilon_c) = 0.058$ is kept equal to the one used for Fig. 4 while the correlation length l_c is increased. We quantify the strength of the clutter (SC) with a single number as:

$$\text{SC} = \sum_{l=1}^N \sum_{\alpha}^{x,y,z} \|\mathbf{f}_{l,\alpha}^{\text{clutter}}\|_{\Gamma}^2. \quad (17)$$

Figure 7(a) shows the evolution of SC with respect to the correlation length for the half-space configuration (solid line) and the homogeneous configuration (dashed line) (corresponding to $\varepsilon_b = 1$).²⁶ When $l_c \ll \lambda$ the clutter can be homogenized which leads to a low scattered field, and when $l_c \gg \lambda$ the large-scale spatial variation of the clutter does not perturb the signal radiated by the targets as it is locally homogeneous. The most disturbing effect of the clutter is expected for correlation lengths corresponding to the maximum of SC. Notice that the behavior of SC with respect to the correlation length differs strongly depending on the

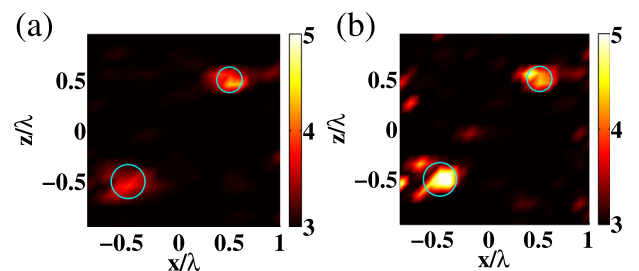


FIG. 6. Same as Figs. 4(a) and 4(b), but the clutter standard variation is increased to $\sigma_f = 0.07$ yielding a CSR of 148% .

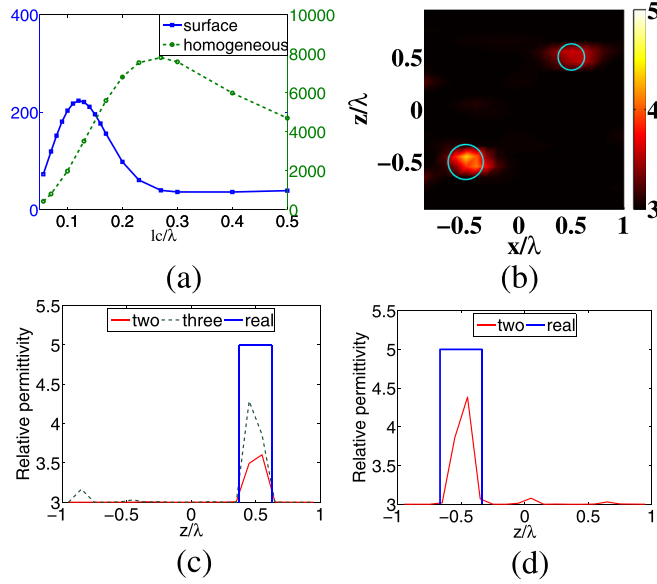


FIG. 7. (a) Strength of the clutter scattered intensity, SC, versus l_c/λ for the half-space configuration (solid line) and for the homogeneous configuration (dashed line). (b)–(d) Reconstructed permittivity obtained with HDORTM and a frequency hopping procedure using only $\lambda_3 = 3\lambda_{\text{ref}}$ and $\lambda_2 = 1.5\lambda_{\text{ref}}$. The clutter is defined by a correlation length $l_c = 0.1\lambda_{\text{ref}}$ and a standard deviation $\sigma_f = 0.058$ (b) Cut in the (x, z) plane for $y = 0.4\lambda_{\text{ref}}$. (c) Reconstructed permittivity with respect to z at $x = 0.5\lambda_{\text{ref}}$ and $y = 0.4\lambda_{\text{ref}}$. The blue solid curve denotes the actual permittivity of the targets, the red dashed line corresponds to the reconstructed profile obtained with HDORTM and a frequency hopping procedure restricted to $\lambda_3 = 3\lambda_{\text{ref}}$ and $\lambda_2 = 1.5\lambda_{\text{ref}}$. The black line indicates the reconstruction obtained when the data obtained at λ_{ref} for the two incident DORT fields focusing on the target close to the interface are included in the frequency hopping procedure. (d) same as (c) but $x = -0.5\lambda_{\text{ref}}$ and $y = 0.4\lambda_{\text{ref}}$. Note that the black line (not shown) is superposed to the red one.

configuration. In the half-space configuration, the SC curve exhibits a sharp peak centered about $l_c\lambda = 0.1$ while in the homogeneous configuration, the SC curve exhibits a smooth behavior with a maximum at $l_c \approx 0.3\lambda$. Note that reducing the numerical aperture of the imaging system in the homogeneous configuration is not sufficient for retrieving the half-space behavior. From this analysis, one expects the CSR to rocket up at λ_{ref} if the clutter has a correlation length of $l_c = \lambda_{\text{ref}}/10$. Indeed, when $l_c = \lambda_{\text{ref}}/10$ and $\sigma_f = 0.058$, one obtains a CSR equal to 34%, 66%, and 282% for $\lambda_3 = 3\lambda_{\text{ref}}$, $\lambda_2 = 1.5\lambda_{\text{ref}}$, and λ_{ref} , respectively. In this case, due to the high level of noise, the DORT fields at λ_{ref} are not able to focus on the target far from the interface. One obtains only two fields focusing on the target close to the interface. On the other hand, at $\lambda_2 = 1.5\lambda_{\text{ref}}$ and $\lambda_3 = 3\lambda_{\text{ref}}$, the DORT method yields four focusing fields aiming at both targets. The reconstruction obtained with HDORTM and the frequency hopping procedure for $\lambda_2 = 1.5\lambda_{\text{ref}}$ and $\lambda_3 = 3\lambda_{\text{ref}}$ using the four focusing incident fields is displayed in Fig. 7. The two scatterers are well localized but the smallest target close to the interface is under evaluated. Adding the third wavelength λ_{ref} in the frequency hopping procedure with the four incident fields deteriorates the reconstruction (not shown) because the additional data obtained with the third and fourth DORT eigenvectors at λ_{ref} correspond essentially to the clutter signature. Yet, by restricting at λ_{ref} the

incident DORT fields to the first two eigenvectors and running the inversion with an initial guess corresponding to the reconstruction obtained at $1.5\lambda_{\text{ref}}$, one ameliorates the reconstruction of the target close to the interface while leaving unchanged the reconstruction of the target far from the interface, see Fig. 7.

In the last example, we consider a clutter with l_c equal to $0.3\lambda_{\text{ref}}$. As expected in this case, the CSR decreases with the wavelength. It is equal 339%, 64%, and 41% for $\lambda_1 = 3\lambda_{\text{ref}} = 10l_c$, $\lambda_2 = 1.5\lambda_{\text{ref}}$ and λ_{ref} , respectively. The reconstruction obtained with the frequency hopping procedure using the three wavelengths is shown in Figs. 8(a) and 8(c)–8(d) in dashed line. One observes that the scatterer far from the interface is under evaluated and that it is accompanied by ghost objects regularly placed along the z axis. These oscillations indicate that the frequency hopping procedure is not optimal. Indeed, the reconstruction obtained at $3\lambda_{\text{ref}}$ is strongly perturbed by the clutter signature and this noisy initial guess compromises the following inversions. Now, choosing another wavelength for starting the frequency hopping procedure is not easy. Taking a much larger λ , which ensures that the clutter signature is low, yields a poor reconstruction, due to the lack of high spatial frequency information, which is basically useless in the frequency hopping procedure. Similarly, the smaller wavelengths which permit the diminution of SC are too close to $1.5\lambda_{\text{ref}}$ and do not bring additional information. Thus, we decided to keep the same wavelength range $[\lambda_{\text{ref}}, 3\lambda_{\text{ref}}]$ but used a finer

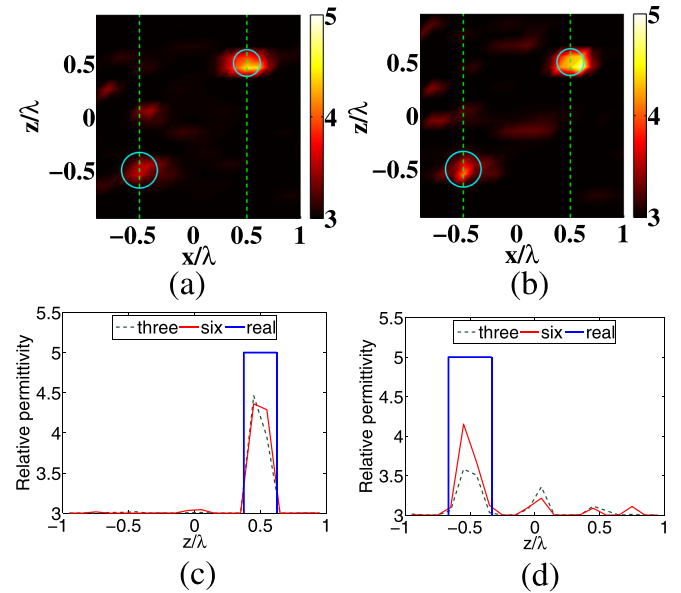


FIG. 8. Reconstructed permittivity obtained with HDORTM when the clutter correlation length is $l_c = 0.3\lambda_{\text{ref}}$ and standard variation $\sigma_f = 0.058$ when three, $3\lambda_{\text{ref}} = 10l_c$, $1.5\lambda_{\text{ref}}$ and λ_{ref} , or six $3\lambda_{\text{ref}}$, $2.5\lambda_{\text{ref}}$, $2\lambda_{\text{ref}}$, $1.5\lambda_{\text{ref}}$, $1.25\lambda_{\text{ref}}$, λ_{ref} wavelengths are used in the frequency hopping procedure. (a) Cut along the (x, z) plane for $y = 0.4\lambda_{\text{ref}}$ of the reconstructed permittivity obtained when three wavelengths are used in the frequency hopping procedure. (b) same as (a) but six wavelengths are used in the frequency hopping procedure. (c) and (d) plot of the relative permittivity versus (c) z for $x = 0.5\lambda_{\text{ref}}$ and $y = 0.4\lambda_{\text{ref}}$; (d) z for $x = -0.5\lambda_{\text{ref}}$ and $y = 0.4\lambda_{\text{ref}}$. The blue solid line denotes the actual profiles of the targets. The dark green dashed lines indicate the reconstruction obtained with three wavelengths. The red solid lines indicate the reconstruction obtained with six wavelengths.

discretization step. When six operating wavelengths, $3\lambda_{\text{ref}}$, $2.5\lambda_{\text{ref}}$, $2\lambda_{\text{ref}}$, $1.5\lambda_{\text{ref}}$, $1.25\lambda_{\text{ref}}$, λ_{ref} , are considered in the frequency hopping procedure, the reconstruction is ameliorated, as seen in Figs. 8(b)–8(d) in solid line. This example points out the limitation of the frequency hopping procedure. Depending on the clutter characteristics, its implementation (choice of the wavelengths, choice of the kept incident fields in the inversion) must be adapted. It is likely that a global multifrequency inversion procedure would lead to better results.

V. CONCLUSION

In conclusion, we have analyzed the performance, on simulated data, of a hybrid-DORT method for localizing and characterizing scatterers buried under a flat interface in a highly cluttered semi-infinite medium. This realistic imaging configuration is plagued by a low numerical aperture due to the impedance matching between the antennas and the host medium.

We have shown that the hybrid-DORT approach, which uses only the data obtained with the DORT incident fields that focus on the strongest scatterers, is always more efficient than the classical inversion technique, which uses the whole data set, for extracting and imaging the targets. Moreover it permits a dramatic reduction of the computation time.

To diminish the reconstruction artifacts stemming from the small effective numerical aperture of the imager, we have considered multifrequency data and implemented a frequency hopping procedure. We have pointed out that the clutter nuisance potential depends strongly on the ratio between the clutter correlation length and the wavelength. The frequency hopping performance depending strongly on the initial reconstruction at low frequency, its strategy (choice of the wavelengths, choice of the DORT incident fields in the inversion procedure) must be adapted to the clutter characteristics.

To avoid the wavelength adjustment of this sequential inversion procedure and ameliorate the reconstruction, a global multifrequency reconstruction approach using the DORT incident fields may be an interesting alternative. Work in this direction is in progress.

¹L. Souriau, B. Duchêne, D. Lesselier, and R. E. Kleinman, “Modified gradient approach to inverse scattering for binary objects in stratified media,” *Inverse Probl.* **12**, 463–481 (1996).

²A. Abubakar and P. M. van den Berg, “Iterative forward and inverse algorithms based on domain integral equations for three-dimensional electric and magnetic objects,” *J. Comput. Phys.* **195**, 236–262 (2004).

³D. H. Liu, G. Kang, L. Li, Y. Chen, S. Vasudevan, W. Joines, Q. H. Liu, J. Krolík, and L. Carin, “Electromagnetic time-reversal imaging of a target in a cluttered environment,” *IEEE Trans. Antennas Propag.* **53**(9), 3058–3066 (2005).

⁴E. Mudry, P. C. Chaumet, K. Belkebir, and A. Sentenac, “Electromagnetic wave imaging of three-dimensional targets using a hybrid iterative inversion method,” *Inverse Probl.* **28**(6), 065007 (2012).

⁵A. Dubois, K. Belkebir, and M. Saillard, “Localization and characterization of two-dimensional targets buried in a cluttered environment,” *Inverse Probl.* **20**(6), S63–S79 (2004).

⁶C. D. Moss, F. L. Teixeira, and J. A. Kong, “Detection of targets in continuous random media: A numerical study using the angular correlation function,” *Microwave Opt. Technol. Lett.* **33**, 242–247 (2002).

⁷O. Cmielewski, M. Saillard, K. Belkebir, and H. Tortel, “On the characterization of buried targets under a rough surface using the wigner-ville transformation,” *IEEE Trans. Geosci. Remote Sens.* **3**, 442–446 (2006).

⁸O. Cmielewski, H. Tortel, A. Litman, and M. Saillard, “A two-step procedure for characterizing obstacles under a rough surface from bistatic measurements,” *IEEE Trans. Geosci. Remote Sens.* **45**, 2850–2858 (2007).

⁹H. Ammari, J. Garnier, and K. Solna, “A statistical approach to target detection and localization in the presence of noise,” *Waves Random Complex Media* **22**(1), 40–65 (2012).

¹⁰M. Fink, C. Prada, F. Wu, and D. Cassereau, “Self focusing with time reversal mirror in inhomogeneous media,” *Proc.-IEEE Ultrason. Symp.* **2**, 681–686 (1989).

¹¹C. Prada and M. Fink, “Eigenmodes of the time reversal operator: a solution to selective focusing in multiple-target media,” *Wave Motion* **20**, 151–163 (1994).

¹²M. Fink, “Time reversed acoustics,” *Phys. Today* **50**(3), 34–40 (1997).

¹³H. Tortel, G. Micolau, and M. Saillard, “Decomposition of the time reversal operator for electromagnetic scattering,” *J. Electromagn. Waves Appl.* **13**, 687–719 (1999).

¹⁴G. Micolau and M. Saillard, “D.O.R.T. method as applied to electromagnetic sensing of buried objects,” *Radio Sci.* **38**, 1038 (2003).

¹⁵F. D. Philippe, C. Prada, D. Clorennec, M. Fink, and T. Folegot, “Construction of the temporal invariants of the time-reversal operator,” *J. Acoust. Soc. Am.* **126**(1), EL8–EL13 (2009).

¹⁶D. Lesselier, E. Iakovleva, S. Gdoura, and G. Perrusson, “Multistatic Response Matrix of a 3-D Inclusion in Half Space and MUSIC Imaging,” *IEEE Trans. Antennas Propag.* **55**(9), 2598–2609 (2007).

¹⁷H. Ammari, E. Iakovleva, D. Lesselier, and G. Perrusson, “Music-type electromagnetic imaging of a collection of small three-dimensional inclusions,” *SIAM J. Sci. Comput. (USA)* **29**(2), 674–709 (2007).

¹⁸A. J. Devaney, E. A. Marengo, and F. K. Gruber, “Time-reversal-based imaging and inverse scattering of multiply scattering point targets,” *J. Acoust. Soc. Am.* **118**(5), 3129–3138 (2005).

¹⁹M. E. Yavuz and F. L. Teixeira, “On the sensitivity of time-reversal Imaging techniques to model perturbations,” *IEEE Trans. Antennas Propag.* **56**(3), 834–843 (2008).

²⁰M. Davy, T. Lepetit, J. de Rosny, C. Prada, and M. Fink, “Detection and imaging of human beings behind a wall using the dort method,” *Prog. Electromagn. Res.* **110**, 353–369 (2010).

²¹L. Bellomo, S. Pioch, M. Saillard, and E. Spano, “Time reversal experiments in the microwave range: description of the radar and results,” *Prog. Electromagn. Res.* **104**, 427–448 (2010).

²²X. Antoine, B. Pincon, K. Ramdani, and B. Thierry, “Far field modeling of electromagnetic time reversal and application to selective focusing on small scatterers,” *SIAM J. Appl. Math.* **69**(3), 830–844 (2008).

²³M. E. Yavuz and F. L. Teixeira, “Electromagnetic fields in dispersive, random inhomogeneous media,” *IEEE Trans. Antennas Propag.* **54**(8), 2305–2315 (2006).

²⁴D. H. Chambers and J. G. Berryman, “Analysis of the time-reversal operator for planar dipole arrays,” in *IEEE Antennas Propag., vol 1-4 2004, Digest*, pp. 679–682. IEEE Antennas & Propagat Soc; Univ Calif, Lawrence Livermore Natl Lab; Northrop Grumman; ITT Ind; ANSOFT, 2004. IEEE Antennas-and-Propagation-Society International Symposium, Monterey, CA, June 20–26, 2004.

²⁵D. H. Chambers and J. G. Berryman, “Analysis of the time-reversal operator for a small spherical scatterer in an electromagnetic field,” *IEEE Trans. Antennas Propag.* **52**(7), 1729–1738 (2004).

²⁶T. Zhang, P. C. Chaumet, E. Mudry, A. Sentenac, and K. Belkebir, “Electromagnetic wave imaging of targets buried in a cluttered medium using a hybrid inversion-dort method,” *Inverse Probl.* **28**(12), 125008 (2012).

²⁷P. C. Chaumet, A. Sentenac, and A. Rahmani, “Coupled dipole method for scatterers with large permittivity,” *Phys. Rev. E* **70**, 036606–6 (2004).

²⁸P. C. Chaumet, K. Belkebir, and A. Sentenac, “Superresolution of three-dimensional optical imaging by use of evanescent waves,” *Opt. Lett.* **29**, 2740–2742 (2004).

²⁹K. Belkebir, P. C. Chaumet, and A. Sentenac, “Superresolution in total internal reflection tomography,” *J. Opt. Soc. Am. A* **22**, 1889–1897 (2005).

³⁰K. Belkebir, S. Bonnard, F. Pezin, P. Sabouroux, and M. Saillard, “Validation of 2D inverse scattering algorithms from multi-frequency experimental data,” *J. Electromagn. Waves Appl.* **14**, 1637–1667 (2000).

³¹K. Belkebir and A. G. Tijhuis, “Modified² gradient method and modified Born method for solving a two-dimensional inverse scattering problem,” *Inverse Probl.* **17**(6), 1671–1688 (2001).

- ³²W. H. Press, B. P. Flannery, S. A. Teukolski, and W. T. Vetterling, *Numerical Recipes. The Art of Scientific Computing* (Cambridge University Press, 1986).
- ³³M. Saillard, P. Vincent, and G. Micolau, "Reconstruction of buried objects surrounded by small inhomogeneities," *Inverse Probl.* **16**, 1195–1208 (2000).
- ³⁴W. C. Chew and J. H. Lin, "A frequency-hopping approach for microwave imaging of large inhomogeneous bodies," *IEEE Microw. Guid. Wave Lett.* **5**(12), 439–441 (1995).
- ³⁵A. Dubois, J. M. Geffrin, K. Belkebir, and M. Saillard, "Imaging of dielectric cylinders from experimental stepped-frequency data," *Appl. Phys. Lett.* **88**(16), 164104 (2006).